Hindawi
Geofluids
Volume 2020, Article ID 1894149, 17 pages
https://doi.org/10.1155/2020/1894149

Research Article

A Unified Multiple Transport Mechanism Model for Gas through Shale Pores

Fanhui Zeng,[1] **Yu Zhang**,[1] **Jianchun Guo**,[1] **Wenxi Ren**,[1] **Tao Zhang**,[1] **Qifeng Jiang**,[2] **and Jianhua Xiang**[3]

[1]*State Key Laboratory of Oil and Gas Reservoir Geology and Exploitation, Southwest Petroleum University, Chengdu, China 610500*
[2]*Key Laboratory of Fluid and Power Machinery, Xihua University, Chengdu, China 610039*
[3]*Engineering Technology Research Institute, Chengdu, China 610017*

Correspondence should be addressed to Fanhui Zeng; zengfanhui023024@126.com

Received 14 February 2020; Revised 17 August 2020; Accepted 19 September 2020; Published 17 October 2020

Academic Editor: Jinze Xu

Predicting apparent gas permeability (AGP) in nanopores is a major challenge for shale gas development. Considering the differences in the gas molecule-pore wall interactions in inorganic and organic nanopores, the gas transport mechanisms in shale remain unclear. In this paper, gas flow channels in shale, which are separated into inorganic pores and organic pores, are treated as nanotubes. Inorganic pores are assumed to be hydrophilic, and organic pores are assumed to be hydrophobic. In organic pores, multiple bulk free gas and surface adsorbed gas transport mechanisms are incorporated, while the bulk gas and water film are considered within inorganic pores. This paper presents a unified multiple transport mechanism model for both organic nanopores and inorganic nanopores. Unlike the earlier models, the presented models consider the absorption, stress dependence, real gas, and water storage effects on gas transport comprehensively for the entire flow regime. The results are validated with published data which is more in line with the real situation. The results show that (1) the AGP decreases gradually as the pore pressure decreases but that the decrease is sharp in small pores, (2) the AGP decreases dramatically when considering the real gas effect at 50 MPa in a 2 nm pore size, and (3) for a small pore size at the critical high-water saturation, AGP might increase suddenly as the flow regime changes from continuum flow to slip flow. The findings of this study can help for better understanding of the gas transport mechanisms for the entire flow regime in shale.

1. Introduction

Shale gas has become increasingly vital in supplying hydrocarbon energy due to its potential to offset conventional gas production declines. A shale gas reservoir typically has nanosized pores, which can be categorized into pores in organic matter (OM) and pores in inorganic matter (IOM) according to the mineral composition, microstructure, and wettability differences [1, 2]. The pores in OM vary in size from nanometer scale to micrometer scale, while those in IOM are on the nanometer scale [3, 4]. Generally, the bulk gas transport capacity and surface diffusion should simultaneously be considered for the coexistence of bulk gas and adsorbed gas phases in organic pores [5]. For the absorbed gas, the adsorption flux decreases as the gas desorbs during depressurization, which increases the organic pore flow channel [6–8]. However, IOM is mainly composed of quartz and clay content, which are prone to absorb water [4, 9]. Hence, bulk gas phases and water films coexist in the pores of IOM [10].

The gas transport in shale nanopores is very different from that due to conventional macropore mechanisms because the molecular free path is comparable to the pore size [11]. The strong interfacial effects between the gas and nanotube walls increase with increasing K_n; consequently, a continuum approach with no-slip boundary conditions is no longer valid [12]. K_n is defined as the ratio of the mean free path of molecules to the flow path aperture [13] and is applied to characterize the gas flow regime as continuum

flow ($0 < K_n < 10^{-3}$), slip flow ($10^{-3} < K_n < 10^{-1}$), transition flow ($10^{-1} < K_n < 10$), and free molecular flow ($10 < K_n$) [14].

A single-nanopore gas transport mechanism investigation is the theoretical basis for AGP modeling of actual core samples, which has attracted widespread attention [15, 16]. Experimental tests and simulations have been applied to model single-nanopore gas transport capacity [14]. It is usually time-consuming and is extremely difficult to perform laboratory gas transport experiments for the nanopore range considering bulk gas, absorbed gas, real gas, and stress dependence, among other multifactor coupling effects. Second, numerical methods, such as molecular simulation via the lattice Boltzmann model (LBM), are powerful tools for studying gas transport behavior. Third, Qiu et al. [17, 18] studied the phase behavior of fluids confined in nanopores through experimental methods and found that the supercritical region of the confined fluid exists in the low pressure range. However, due to the complexity of the rough pore surface slip boundary, most LBM applications to model gas flow require considerable computational resources and time requirements, which is difficult to account for in practical engineering [4].

To overcome the inconvenience of the numerical method, two different analytical multiscale unified models are developed, coupling various flow regimes for shale gas flow through nanopores. The first method is to solve the Navier-Stokes equation directly by incorporating Maxwell's first-/second-order slip velocity slip boundary condition in the form of a rarefaction effect to cover the entire flow regime. Coupling a second-order slip velocity boundary, Beskok [19] derived a unified nanoscale pore gas transport model for all flow regimes on the basis of the Hagen-Poiseuille equation. However, Karniadakis et al. [20] noted that the unified flow model with general slip boundary conditions resulted in a significant error from that obtained through a direct simulation via the Monte Carlo method. To improve the prediction accuracy, Civan [21] introduced a rarefaction coefficient into the unified equation; this coefficient varies with K_n and can be determined by numerical or experimental data. Following this concept, several investigators [22, 23] further extended the model by incorporating shale gas transport mechanism differences in the OM and IOM. Although the prediction accuracy improved by the introduction of the rarefaction coefficient, the second-order model slip boundary condition is unable to model gas through porous media, while the first-order model is also valid in the low-moderate K_n number regime [24].

Another approach that expresses the shale gas transport capacity by different equations based on the K_n number was proposed. In this approach, the transition flow capacity is superimposed by slip flow and free molecule flow through their weighting coefficients. Adzumi [25] performed experiments on gas transport in circular capillaries, and a contribution coefficient term was applied to express the transition flow regime involvement of viscous flow and Knudsen's flow. However, these models did not provide the contribution coefficient. Javadpour [26] directly superposed the gas transport capacity of slip flow and Knudsen diffusion to develop an AGP model. Furthermore, Darabi [27] introduced the fractal dimension into Knudsen diffusion to consider the pore surface roughness effect based on Javadpour's model, although both models ignored the gas transition flow regime transport capacity.

To directly overcome the limitation of flow capacity summation, several investigators introduced contribution coefficients to fuse different flow regimes. Wu et al. [28] utilized the weighting coefficient expressed by the molecular collision frequency to model gas slip flow and Knudsen diffusion transport capacity for the entire flow regime. Zeng et al. [29, 30] extended this model by directly incorporating surface effects. Chai et al. [23] integrated real gas effects, gas desorption, surface diffusion, etc., to propose a comprehensive gas transport model. However, these models consider that all the flow states coexist and ignore the gas flow state as determined by K_n [14] and the absorbed water film effect. In addition, under the high-temperature and high-pressure conditions of formations in actual gas-shale reservoirs, the assumption that gas molecules can be represented as a point is inappropriate due to the size of gas molecules compared to that of nanopores, and the real gas effect should be considered [27, 31]. In addition, Ross and Bustin [32, 33], after analyzing porosity and permeability test results, reported that shale gas sample permeability was highly stress-dependent, which further complicates shale gas transport.

Overall, the currently established models are unable to consider all the above transport mechanisms and fail to consider shale gas flow capacity differences between organic and inorganic pores. It is urgent to develop a fully coupled unified single-nanopore AGP model for shale gas, merging all the aforementioned gas transport mechanisms. This paper develops a simple but rigorous method to model the transport of shale gas through nanopores via various flow regimes. The remaining parts of this paper are organized as follows: the mathematical modeling is presented in Section 2. The model comparison and validation are presented in Section 3. The effects of the storage medium and pore size, stress dependence, real gas, surface diffusion, and water storage on the AGP are investigated in Section 4. Finally, several conclusions are provided in Section 5. Due to the complexity of considering multiphase flow, this paper does not consider the flow capacity of shale fluids in the presence of multiphase flow.

2. Mathematical Modeling

In the physical model, we consider bulk gas and adsorbed gas phases in organic pores and bulk gas and adsorbed water phases in inorganic pores, as shown in Figure 1.

2.1. Bulk Gas Transport Mechanisms. K_n is usually used to characterize shale gas flow regimes [34].

$$K_n = \frac{\lambda}{d}, \tag{1}$$

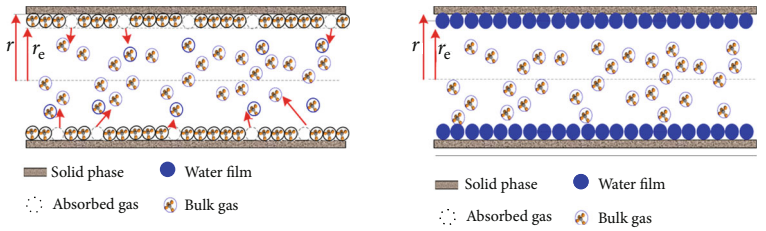

(a) Absorbed gas inside a nanopore in OM (b) Absorbed water inside a nanopore in IOM

Figure 1: Illustration of absorbed gas/water inside shale nanopores.

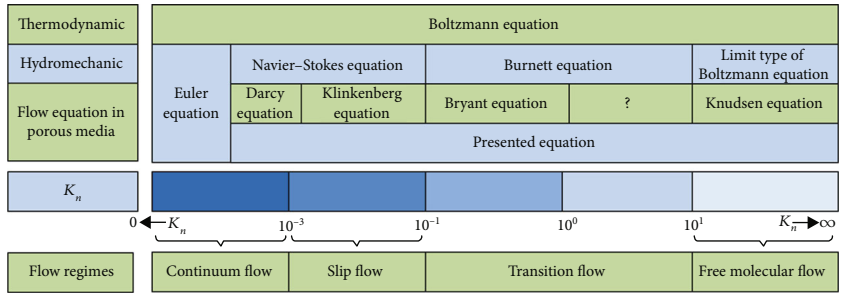

Figure 2: Illustration of flow regimes and corresponding equations [14].

where λ is the molecular mean free path, m, and d is the effective radius of the nanopores, m.

The following equation is used to determine the mean free path:

$$\lambda(p, T) = \frac{k_B T}{\sqrt{2}\pi\delta^2 p}, \tag{2}$$

where k_B is the Boltzmann constant, 1.3805×10^{-23} J/K; T is the formation temperature, K; δ is the gas molecule collision diameter, nm (the value of which is 0.42 nm for CH_4); and p is pore pressure, MPa.

Substituting Equation (2) into Equation (1), one can obtain a more detailed expression of K_n for the gas:

$$K_n(p, T) = \frac{k_B T}{\sqrt{2}\pi\delta^2 p} \cdot \frac{1}{d}. \tag{3}$$

The gas transport mechanism is controlled by different equations for each flow regime according to K_n, as shown in Figure 2. We will derive unified multiple transport mechanism models for the entire flow regime in the following section.

2.1.1. Continuum Flow. The gas transport regime in pores is continuous flow when $K_n < 10^{-3}$. The number of collisions between the gas molecules and pore wall is assumed to be negligible, and the gas flow rate can be expressed by Hagen-Poiseuille's equation ([35]):

$$J_{\text{vicious}} = -\rho \cdot \frac{k_\infty}{\mu} \cdot \nabla p = -\rho \cdot \frac{r^2}{8\mu} \cdot \nabla p, \tag{4}$$

where J_{vicious} is the continuum flow volume flux, kg/(m^2·s); ρ is the gas density, kg/m^3; k_∞ is the intrinsic permeability, m^2; μ is the gas viscosity, Pa·s; r is the nanopore radius, m; p is the pore pressure, Pa; and ∇ is the pressure gradient operator symbol.

2.1.2. Slip Flow. The gas transport regime in pores is continuous flow with a slippage effect when $10^{-3} < K_n < 10^{-1}$. In this regime, the gas velocity near the pore wall is no longer zero due to the slippage effect, which satisfies Klinkenberg's equation. Therefore, the AGP for slip flow can be written as [36] follows:

$$k_{\text{slip}} = k_\infty \cdot \left(1 + \frac{b_k}{p_{\text{aver}}}\right), \tag{5}$$

where k_{slip} is the slip flow regime AGP, m^2; b_k is the gas slip factor, MPa; and p_{aver} is the gas phase mean pressure, MPa, which is equal to the pore pressure.

b_k is defined as [27, 37]

$$b_k = \left(\frac{8\pi RT}{M}\right)^{0.5} \cdot \frac{\mu}{r} \cdot \left(\frac{2}{\alpha} - 1\right), \tag{6}$$

where R is the universal gas constant, J/(mol·K), which is 8314 J/(kmol/K); M is the molar mass, kg/mol; and α is the tangential momentum accommodation coefficient (TMAC), dimensionless.

By inserting Equation (6) into Equation (5), one can obtain the AGP correction form that takes into account the slippage effect:

$$k_{\text{slip}} = k_\infty \cdot \left[1 + \left(\frac{8\pi RT}{M}\right)^{0.5} \cdot \frac{\mu}{p_{\text{avg}} r} \cdot \left(\frac{2}{\alpha} - 1\right)\right]. \tag{7}$$

By substituting (7) into (4), one can obtain

$$J_{\text{slip}} = -\rho \cdot \frac{k_{\text{slip}}}{\mu} \cdot \nabla p = -\rho \cdot \frac{r^2}{8\mu} \cdot \left[1 + \left(\frac{8\pi RT}{M}\right)^{0.5} \cdot \frac{\mu}{p_{\text{avg}} r} \cdot \left(\frac{2}{\alpha} - 1\right)\right] \cdot \nabla p, \tag{8}$$

where J_{slip} is the volume flux for the slip regime, kg/(m^2·s).

2.1.3. Free Molecule Flow. The gas transport regime is free molecule flow when $K_n > 10$. The collision between the gas molecules and the pore walls is the most important influencing factor, and the gas transport satisfies Knudsen diffusion, which can be expressed as [38, 39]

$$J_{\text{Knudsen}} = \frac{M}{ZRT} \cdot D_{\text{k}} \cdot \nabla p, \tag{9}$$

where J_{Knudsen} is the volume flux for the slip regime, kg/(m^2·s); D_{k} is the Knudsen diffusion constant, m^2/s; and Z is the deviation factor.

Additionally, the Knudsen diffusion constant can be written as [14, 26]

$$D_{\text{k}} = \frac{2r}{3} \cdot \left(\frac{8RT}{\pi M}\right)^{0.5}. \tag{10}$$

During the gas flow in nanopores, the wall roughness has a profound effect on the Knudsen diffusion constant. The effective Knudsen diffusion constant influenced by roughness can be written as [27, 40]

$$D_{\text{eff-k}} = \left(\frac{d_{\text{m}}}{d}\right)^{D_{\text{f}}\text{-}2} \cdot D_{\text{k}}, \tag{11}$$

where $D_{\text{eff-k}}$ is the effective Knudsen diffusion constant, m^2/s; d_{m} is the gas molecule diameter; and D_{f} is the pore wall fractal dimension, dimensionless.

Substituting Equations (10) and (11) into Equation (9), the Knudsen diffusion incorporating pore wall roughness can be written as

$$J_{\text{Knudsen}} = \frac{M}{ZRT} \cdot \frac{2r}{3} \cdot \left(\frac{d_{\text{m}}}{d}\right)^{D_{\text{f}}\text{-}2} \cdot \left(\frac{8RT}{\pi M}\right)^{0.5} \nabla p. \tag{12}$$

2.1.4. Transition Flow. For $10^{-1} < K_n < 10$, the momentum transfer of molecules between the pore walls is important, and the continuous flow and Knudsen flow mechanisms coexist under such conditions [41]. It is vital to calculate the comprehensive apparent permeability through reasonable weighting coefficients of both gas transport mechanisms together. Considering gaseous mixtures flowing through capillaries simultaneously under continuum flow and Knudsen diffusion, Adzumi [42] introduced a contribution coefficient term ε to express each of the flow regimes involved in gas transport:

$$J_{\text{t}} = J_{\text{vicious}} + \varepsilon J_{\text{Knudsen}}, \tag{13}$$

where J_{t} is the volume flux, kg/(m^2·s), and ε is the contribution coefficient term, dimensionless.

Adzumi [42] noted that the value of ε varies between 0.7 and 1.0 smoothly. Unfortunately, Adzumi [42] did not explain how to obtain the specific value ε in his experiments. Based on Adzumi's research, Mohammad [43] expressed the total mass flow as a superposition of the viscous flow and free molecular flow as follows:

$$J_{\text{t}} = (1\text{-}\varepsilon) J_{\text{vicious}} + \varepsilon J_{\text{Knudsen}}. \tag{14}$$

To reflect the flow difference results for different regimes, the following equation is applied to provide reasonable results that vary with the Knudsen number for all the flow regimes ([43]):

$$\varepsilon = C_{\text{A}} \left[1 - \exp\left(\frac{-K_n}{K_{n\text{Viscous}}}\right)\right]^s, \tag{15}$$

where C_{A} and S are constants, dimensionless, which are 1; $K_{n\text{Viscous}}$ equals K_n when the flow regime transfers from viscous to diffusion flow, which is usually set as 0.3. The simulation results show that Equation (15) fit the Monte Carlo simulation data well, which is much better than Beskok's model with the first-/second-order model slip boundary [34].

Obviously, the slip effect is not considered in Equation (14). We propose a modification of Equation (14) in this paper:

$$J_{\text{t}} = (1\text{-}\varepsilon) J_{\text{slip}} + \varepsilon J_{\text{Knudsen}}. \tag{16}$$

2.2. Absorbed Gas Transport Mechanisms

2.2.1. Gas Desorption. For the absorbed gas, the adsorption layer thickness decreases as the gas desorbs during depressurization, which increases the organic pore radius, as shown in Figure 1(a). The modified Langmuir adsorption isotherm equation is adopted to model this effect ([39]):

$$V = V_{\text{L}} \cdot \theta, \tag{17}$$

$$\theta = \frac{p/Z}{p/Z + p_{\text{L}}}, \tag{18}$$

where V is the adsorbed gas volume per shale unit weight under standard conditions, m^3/kg; V_{L} is the Langmuir volume under standard conditions, m^3/kg; θ is the gas coverage under certain pressures, dimensionless; and p_{L} is the Langmuir pressure, Pa.

The absorbed gas in the organic matter inner wall recedes the pore flow radius as

$$r_{\text{ef\_or}} = r_{\text{e\_or}} - \theta \cdot d_{\text{m}}, \tag{19}$$

where $r_{\text{ef\_or}}$ is the effective pore flow radius considering gas desorption, m, and $r_{\text{e\_or}}$ is the original pore radius of the organic pore, m.

2.2.2. Surface Diffusion. Surface diffusion is a complicated process of adsorbed phase transport that can be categorized into adatom and cluster diffusion [38]. Several different mathematical models have been presented to express the surface diffusion phenomenon. In this paper, it is assumed that the adsorption and desorption processes would reach equilibrium instantly, which satisfies the Langmuir equation requirement:

$$J_{\text{surface}} = -M \cdot D_s \cdot \frac{C_{s\ \max} p_L}{(p + p_L)^2} \cdot \nabla p, \tag{20}$$

where D_s is the coefficient surface diffusion, m^2/s, and C_{smax} is the maximum adsorption concentration, mol/m^3.

2.3. Multifactorial Effect Mechanisms

2.3.1. Stress Dependence Effect. The effective confining pressure will increase during shale gas depressurization, which will reduce the nanopore porosity and permeability. The following power law equations can be obtained ([44]):

$$k = k_0 \left(\frac{p_e}{p_o}\right)^{-s}, \tag{21}$$

$$\varphi = \varphi_0 \left(\frac{p_e}{p_o}\right)^{-q}, \tag{22}$$

where s and q are the material constants, dimensionless, which can be obtained by permeability and porosity laboratory experiments under different effective pressures; k is the permeability considering the effective stress, μm^2; k_0 is the permeability under the condition of atmospheric pressure, μm^2; p_e is the effective stress, MPa (i.e., p_c-p); p_c is the confining pressure, MPa; p_0 is the atmospheric pressure, MPa; φ is the porosity under the effective stress, dimensionless; and φ_0 is the porosity at atmospheric pressure, dimensionless.

For capillary nanotubes, the relationship between the nanopore radius and intrinsic permeability can be written as [45]

$$r = 2\sqrt{2\tau}\sqrt{\frac{k}{\varphi_0}}. \tag{23}$$

Following Equations (21)–(23), the pore effective radius considering the stress dependence effect can be written as

$$r_{ef} = r\left(\frac{p_e}{p_o}\right)^{0.5(q-s)}, \tag{24}$$

where r_{ef} is the effective flow radius considering the stress dependence effect, m.

2.3.2. Water Storage Characteristics within Inorganic Nanopores. The shale clay layer minerals with additional negatively charged electrostatic properties are prone to cause the water molecules to adsorb onto the interpore surface under actual reservoir conditions. The water film formation will reduce the inorganic pore effective radius shown in Figure 1(b), and one can obtain the following water saturation equation:

$$s_w = \frac{v_w}{v_p} = \frac{\pi r_{e\_in}^2 l_c - \pi r_{eff\_in}^2 l_c}{\pi r_{e\_in}^2 l_c} = \frac{r_{e\_in}^2 - r_{eff\_in}^2}{r_{e\_in}^2}. \tag{25}$$

Rearranging Equation (25) gives the relationship between r_{eff_in} and r_{ef_in}:

$$r_{eff\_in} = r_{ef\_in}\sqrt{1\text{-}s_w}, \tag{26}$$

where s_w is the shale pore water saturation, dimensionless; v_w and v_p are the bound water volume and pore volume, respectively, m^3; r_{e_in} is the hydrodynamic radius for inorganic pores taking the stress dependence effect into account, m; r_{eff_in} is the inorganic pore effective flow radius considering the stress dependence effect and water storage characteristics, m; and l_c is the capillary length, m.

2.3.3. Real Gas Physical Properties. The mutual force and volume of gas molecules should be considered for evaluating shale gas reservoirs under realistic high-pressure and high-temperature conditions. The real gas effect, due to the gas compressibility factor and gas viscosity, is different from that under ideal conditions and should be considered carefully. Here, we apply pseudopressure and pseudotemperature to determine the gas compressibility factor ([39]):

$$Z = 0.702 p_r^2 e^{-2.5T_r}\text{-}5.524 p_r e^{-2.5T_r} + 0.044 T_r^2\text{-}0.164 T_r + 1.15, \tag{27}$$

$$p_r = \frac{p}{p_c}, \tag{28}$$

$$T_r = \frac{T}{T_c}, \tag{29}$$

where p_r is the pseudopressure, dimensionless; T_r is the pseudotemperature, dimensionless; p_c is the critical pressure, MPa; and T_c is the critical temperature, K.

The effective viscosity for gas transport in nanopores can be presented as [46]

$$\mu_{\text{eff}} = \left(1 \times 10^{-7}\right) K_d \exp\left(X \rho^Y\right), \tag{30}$$

$$K_d = \frac{(9.379 + 0.01607M) T^{1.5}}{(209.2 + 19.26M + T)}, \tag{31}$$

$$\rho = 1.4935 \times 10^{-3} \frac{pM}{ZT}, \tag{32}$$

$$X = 3.448 + \frac{986.4}{T} + 0.01009M, \tag{33}$$

$$Y = 2.447 - 0.2224X, \tag{34}$$

where μ_{eff} is the effective viscosity of the gas transport in nanopores, Pa·s; K_d is the intermediate variable of the viscosity calculation, dimensionless; ρ is the gas density, kg/m^3; X is the density multiplication factor, dimensionless; and Y is the density index, dimensionless.

2.4. The Coupling Transport Mechanism for Organic/Inorganic Nanopores. In this section, we build unified AGP models for modeling gas transport through nanopores with various values of K_n; these models are valid for modeling the entire flow regime and take multiple transport mechanisms into account. The presented models also consider the difference in the flow mechanism between organic and inorganic nanopores.

2.4.1. The AGP Model for Organic Nanopores. The total mass flux is determined by the bulk gas and adsorbed gas phases of the organic pores. The flow capacity equation can be written as follows according to the value of K_n.

(1) *Continuum Flow* ($K_n < 10^{-3}$). The bulk gas AGP is obtained through the linear superposition of the continuum flow formula and surface diffusion formula:

$$k_{\text{app\_or1}} = \frac{\left(r_{eff\_\text{or}} - \theta \cdot d_{\text{m}}\right)^2}{8} + M \cdot D_{\text{s}} \cdot \frac{C_{\text{s max}} p_{\text{L}}}{\left(p + p_{\text{L}}\right)^2} \cdot \frac{\mu_{\text{eff}}}{\rho}, \tag{35}$$

where r_{eff_or} is the effective flow radius for organic pores considering gas desorption and the stress dependence effect, m.

(2) *Slip Flow* ($10^{-3} < K_n < 10^{-1}$). The AGP of bulk gas due to the updated Klingenberg effect formula and the surface diffusion formula is obtained through their linear superposition:

$$\begin{aligned} k\text{app\_or2} = {} & \frac{\left(r_{eff\_\text{or}} - \theta \cdot d_{\text{m}}\right)^2}{8} \left[1 + \left(\frac{8\pi RT}{M}\right)^{0.5} \right. \\ & \left. \cdot \frac{\mu_{\text{eff}}}{p_{\text{avg}}\left(r_{eff\_\text{or}} - \theta \cdot d_{\text{m}}\right)} \cdot \left(\frac{2}{\alpha} - 1\right)\right] \\ & + M \cdot D_{\text{s}} \cdot \frac{C_{\text{s max}} p_{\text{L}}}{\left(p + p_{\text{L}}\right)^2} \cdot \frac{\mu_{\text{eff}}}{\rho}. \end{aligned} \tag{36}$$

(3) *Free Molecule Flow* ($K_n > 10$). The bulk gas AGP due to Knudsen flow and absorbed gas surface diffusion is given as

$$\begin{aligned} k\text{app\_or3} = {} & \frac{M}{ZRT} \cdot \frac{2\left(r_{eff\_\text{or}} - \theta \cdot d_{\text{m}}\right)}{3} \\ & \cdot \left(\frac{d_{\text{M}}}{2\left(r_{eff\_\text{or}} - \theta \cdot d_{\text{m}}\right)}\right)^{D_{\text{f}}\text{-}2} \cdot \left(\frac{8RT}{\pi M}\right)^{0.5} \\ & \cdot \frac{\mu_{\text{eff}}}{\rho} + M \cdot D_{\text{s}} \cdot \frac{C_{\text{s max}} p_{\text{L}}}{\left(p + p_{\text{L}}\right)^2} \cdot \frac{\mu_{\text{eff}}}{\rho}. \end{aligned} \tag{37}$$

(4) *Transition flow* ($10^{-1} < K_n < 10$). The AGP of bulk gas due to slip flow and free molecule flow, considering the surface diffusion formula, is given as

$$\begin{aligned} k\text{app\_or4} = {} & \frac{\left(r_{eff\_\text{or}} - \theta \cdot d_{\text{m}}\right)^2}{8} \cdot \left[\left(\frac{8\pi RT}{M}\right)^{0.5} \right. \\ & \left. \cdot \frac{\mu_{\text{eff}}}{p_{\text{avg}}\left(r_{\text{ep}} - \theta \cdot d_{\text{m}}\right)} \cdot \left(\frac{2}{\alpha} - 1\right)\right] \\ & \cdot (1 - \varepsilon) + \frac{2\left(r_{eff\_\text{or}} - \theta \cdot d_{\text{m}}\right)}{3} \cdot \left(\frac{8\text{R}T}{\pi M}\right)^{0.5} \\ & \cdot \frac{\mu_{\text{eff}}}{\rho} \cdot \varepsilon + M \cdot D_{\text{s}} \cdot \frac{\mu_{\text{eff}}}{\rho} \cdot \frac{C_{\text{s max}} p_{\text{L}}}{\left(p + p_{\text{L}}\right)^2}. \end{aligned} \tag{38}$$

2.4.2. The AGP Model for Inorganic Nanopores. The AGP for inorganic nanopores is determined by the bulk gas transport mechanisms and water film properties. Considering the stress dependence and real gas effect, the AGP for inorganic pores can be written as

(1) *Continuum Flow* ($K_n < 10^{-3}$)

$$k\text{app\_in1} = \frac{r_{\text{eff\_in}}^2}{8} \tag{39}$$

(2) *Slip Flow* ($10^{-3} < K_n < 10^{-1}$)

$$k\text{app\_in2} = \frac{r_{\text{eff\_in}}^2}{8} \left[1 + \left(\frac{8\pi RT}{M}\right)^{0.5} \cdot \frac{\mu_{\text{eff}}}{p_{\text{avg}} r_{\text{eff\_in}}} \cdot \left(\frac{2}{\alpha} - 1\right)\right] \tag{40}$$

(3) *Free Molecule Flow* ($K_n > 10$)

$$k_{\text{app\_in3}} = \frac{2r_{\text{eff\_in}}}{3p_{\text{avg}}} \cdot \left(\frac{d_{\text{m}}}{2r_{\text{eff\_in}}}\right)^{D_{\text{f}}\text{-}2} \cdot \frac{8RT^{0.5}}{\pi M} \cdot \frac{\mu_{\text{eff}}}{\rho} \tag{41}$$

(4) *Transition Flow* ($10^{-1} < K_n < 10$)

$$\begin{aligned} k_{\text{app\_in4}} = {} & \frac{r_{\text{eff\_in}}^2}{8} \cdot \left[\left(\frac{8\pi RT}{M}\right)^{0.5} \cdot \frac{\mu_{\text{eff}}}{p_{\text{avg}} r_{\text{eff\_in}}} \cdot \left(\frac{2}{\alpha} - 1\right)\right] \cdot (1 - \varepsilon) \\ & + \frac{2r_{\text{eff\_in}}}{3p_{\text{avg}}} \cdot \left(\frac{d_{\text{m}}}{d}\right)^{D_{\text{f}}\text{-}2} \cdot \left(\frac{8\text{R}T}{\pi M}\right)^{0.5} \cdot \frac{\mu_{\text{eff}}}{\rho} \cdot \varepsilon \end{aligned} \tag{42}$$

2.5. The AGP Model for Organic/Inorganic Nanopores. The final AGP equations for organic and inorganic pores can be obtained through the apparent liquid phase permeability model of organic pores and inorganic pores established in Section 2.4.

(1) *The AGP Model For Organic*

$$\begin{cases} k_{\text{app\_or1}} = \dfrac{\left(r_{eff\_\text{or}} - \theta \cdot d_{\text{m}}\right)^2}{8} + M \cdot D_{\text{s}} \cdot \dfrac{C_{\text{s max}} p_{\text{L}}}{\left(p + p_{\text{L}}\right)^2} \cdot \dfrac{\mu_{\text{eff}}}{\rho}, & \text{Continuum flow } \left(K_n < 10^{-3}\right), \\ k\text{app\_or2} = \dfrac{\left(r_{eff\_\text{or}} - \theta \cdot d_{\text{m}}\right)^2}{8}\left[1 + \left(\dfrac{8\pi RT}{M}\right)^{0.5} \cdot \dfrac{\mu_{\text{eff}}}{p_{\text{avg}}\left(r_{eff\_\text{or}} - \theta \cdot d_{\text{m}}\right)} \times \left(\dfrac{2}{\alpha} - 1\right)\right] + M \cdot D_{\text{s}} \cdot \dfrac{C_{\text{s max}} p_{\text{L}}}{\left(p + p_{\text{L}}\right)^2} \cdot \dfrac{\mu_{\text{eff}}}{\rho}, & \text{Slip flow } \left(10^{-3} < K_n < 10^{-1}\right), \\ k\text{app\_or3} = \dfrac{M}{ZRT} \cdot \dfrac{2\left(r_{eff\_\text{or}} - \theta \cdot d_{\text{m}}\right)}{3} \cdot \left(\dfrac{d_{\text{M}}}{2\left(r_{eff\_\text{or}} - \theta \cdot d_{\text{m}}\right)}\right)^{D_{\text{f}}\text{-}2} \times \left(\dfrac{8\text{R}T}{\pi M}\right)^{0.5} \cdot \dfrac{\mu_{\text{eff}}}{\rho} + M \cdot D_{\text{s}} \cdot \dfrac{C_{\text{s max}} p_{\text{L}}}{\left(p + p_{\text{L}}\right)^2} \cdot \dfrac{\mu_{\text{eff}}}{\rho}, & \text{Free molecule flow } \left(K_n > 10\right), \\ k\text{app\_or4} = \dfrac{\left(r_{eff\_\text{or}} - \theta \cdot d_{\text{m}}\right)^2}{8} \cdot \left[\left(\dfrac{8\text{R}T}{\pi M}\right)^{0.5} \cdot \dfrac{\mu_{\text{eff}}}{p_{\text{avg}}\left(r_{\text{ep}} - \theta \cdot d_{\text{m}}\right)} \cdot \left(\dfrac{2}{\alpha} - 1\right)\right] \cdot (1 - \varepsilon) + \dfrac{2\left(r_{eff\_\text{or}} - \theta \cdot d_{\text{m}}\right)}{3} \cdot \left(\dfrac{8\text{R}T}{\pi M}\right)^{0.5} \cdot \dfrac{\mu_{\text{eff}}}{\rho} \cdot \varepsilon + M \cdot D_{\text{s}} \cdot \dfrac{\mu_{\text{eff}}}{\rho} \cdot \dfrac{C_{\text{s max}} p_{\text{L}}}{\left(p + p_{\text{L}}\right)^2}, & \text{Transition flow } \left(10^{-1} < K_n < 10\right) \end{cases} \tag{43}$$

(2) *The AGP model for Inorganic*

$$\begin{cases} k\text{app\_in1} = \dfrac{r_{\text{eff\_in}}^2}{8}, & \text{Continuum flow } \left(K_n < 10^{-3}\right), \\ k\text{app\_in2} = \dfrac{r_{\text{eff\_in}}^2}{8}\left[1 + \left(\dfrac{8\pi RT}{M}\right)^{0.5} \cdot \dfrac{\mu_{\text{eff}}}{p_{\text{avg}} r_{\text{eff\_in}}} \cdot \left(\dfrac{2}{\alpha} - 1\right)\right], & \text{Slip flow } \left(10^{-3} < K_n < 10^{-1}\right), \\ k_{\text{app\_in3}} = \dfrac{2r_{\text{eff\_in}}}{3p_{\text{avg}}} \cdot \left(\dfrac{d_{\text{m}}}{2r_{\text{eff\_in}}}\right)^{D_{\text{f}}\text{-}2} \cdot \left(\dfrac{8RT}{\pi M}\right)^{0.5} \cdot \dfrac{\mu_{\text{eff}}}{\rho}, & \text{Free molecule flow } \left(K_n > 10\right), \\ k_{\text{app\_in4}} = \dfrac{r_{\text{eff\_in}}^2}{8} \cdot \left[\left(\dfrac{8\pi RT}{M}\right)^{0.5} \cdot \dfrac{\mu_{\text{eff}}}{p_{\text{avg}} r_{\text{eff\_in}}} \cdot \left(\dfrac{2}{\alpha} - 1\right)\right] \cdot (1 - \varepsilon) + \dfrac{2r_{\text{eff\_in}}}{3p_{\text{avg}}} \cdot \left(\dfrac{d_{\text{m}}}{d}\right)^{D_{\text{f}}\text{-}2} \cdot \left(\dfrac{8RT}{\pi M}\right)^{0.5} \cdot \dfrac{\mu_{\text{eff}}}{\rho} \cdot \varepsilon, & \text{Transition flow } \left(10^{-1} < K_n < 10\right) \end{cases} \tag{44}$$

3. Model Comparison and Validation

Validation of the presented AGP models is demonstrated in this section. The coupled models established in this paper are compared with the models proposed by Xiong et al. [47], Asana et al. [48], and Song et al. [11], as shown in Table 1.

Table 1 clearly shows that the AGP models presented by Xiong et al. and Asana et al. incorporate free gas and surface diffusions to model gas transport. However, they ignore the phase behavior influence on the gas viscosity, stress dependence, desorption, and water storage effects on pore diameter. In their models, the apparent gas permeability is irrespective of K_n. Although Song et al.'s model considers the difference in the free gas and adsorbed gas transport properties between the organic and inorganic pores, it ignores the effect of nanopore diameter on water storage. The presented models are rather general, assuming that real shale is composed of both organic and inorganic matters. The presented models are capable of modeling adsorbed gas in organic nanopores and adsorbed water films in inorganic nanopores, and the stress dependence and real gas effects are incorporated to more closely reflect the actual reservoir conditions, unlike in the previously established models.

Inputting the basic parameters listed in Table 2, the AGP for different models over the entire K_n range are calculated and shown in Figure 3.

Figure 3 illustrates the AGP of organic and inorganic pores versus pressure results from the presented model compared with those of Song et al.'s, Asana et al.'s, and Xiong et al.'s models for organic and inorganic nanopores. The presented model calculation results fit well with those of Song et al.'s, Asana et al.'s, and Xiong et al.'s models for organic and inorganic nanopores when $K_n < 0.1$. The presented model also fits well with Asana et al.'s model in the range of $0.1 < K_n < 1$ for an organic nanopore, while the presented model achieves the same trend as that of Song et al.'s model for an organic nanopore when $K_n > 0.1$, which indicates that the presented model is valid. Notably, for values of K_n greater than 0.1, one interesting phenomenon exhibited in Figure 3(a) is that the AGP determined by Song et al.'s model shows a sudden increasing trend. The reason for this change is that Song et al.'s model is modified from Beskok-

Table 1: Model comparison.

Case	Apparent permeability model	Description
Xiong et al.'s model	$K_{ad} = K_a + D\mu(MC_{a\ max}p_L/(p+p_L))\left(1 - R_{eff}^2/R_h^2\right)$	Considers only free gas flow and surface diffusion, without considering stress dependence, real gas effects, and water storage characteristics
Asana et al.'s model	$K_{gas} = K_m + \mu D c_g + \mu D_s\left(V_{sL}\rho_{grain}B_g/\varepsilon_{ks}\right)\left(p_L/(p+p_L)^2\right)$	Considers only free flow and surface diffusion
Song et al.'s model	$k_{app\_or} = \left(r_{eff}^2/8\right)\left[1 + \left(128/15\pi^2\right)\tan^{-1}\left(4.0K_n^{0.4}\right)K_n\right] \times (1 + (4K_n/1 + K_n)) + \mu M_g D_s C_{max}(d\theta/dp) \times \left[1 - (r_{eff}/r_{eff\_stress})^2\right]$, $k_{app\_in} = \left(r_{eff}^2/8\right)\left[1 + \left(128/15\pi^2\right)\tan^{-1}\left(4.0K_n^{0.4}\right)K_n\right] \times (1 + (4K_n/1 + K_n))\left[1 - (r_{eff}/r_{eff\_stress})^2\right]$	Considers only free gas flow and surface diffusion, without considering water storage characteristics
Presented models	See Section 2.5	Consider multiple transport mechanisms in organic/inorganic nanopores, stress dependence, real gas effects, adsorption/desorption, and water storage characteristics

Table 2: Basic simulation data.

Parameter name	Symbol	Unit	Numerical value
Gas type	CH_4	—	—
Ideal gas constant	R	J/(mol·K)	8.314
Temperature	T	K	412
Molecular weight	M_{gas}	kg/mol	1.6×10^{-2}
Gas viscosity	μ	Pa·s	1.76×10^{-5}
Nanopore diameter	d	nm	0.35~1010
Rarefaction coefficient	α	Dimensionless	0.8
Gas molecular diameter	d_m	m	0.34×10^{-9}
Confining pressure	p_{con}	Pa	61.8×10^6
Mean formation pressure	p_{avg}	Pa	30.9×10^6
Atmospheric pressure	p_{at}	Pa	101300
Maximum adsorbed gas concentration	C_{smax}	mol/m^3	24080
Langmuir pressure	p_L	MPa	2.38
Surface diffusion coefficient	D_s	m^2/s	2.73×10^{-10}
Material constant	q	Dimensionless	0.04
Material constant	s	Dimensionless	0.08
Porosity	φ	Dimensionless	0.047
Critical pressure	p_c	Pa	4.834×10^{-6}
Critical temperature	T_c	K	150.86
Nanopore surface roughness	D_f	Dimensionless	2.5
Grain density	ρ_{grain}	Lbm/ft^3	166
Langmuir volume	V_{sl}	scf/ton	50
Pore compressibility	C_g	1/psi	3×10^{-6}
Water saturation	s_w	Dimensionless	0.3

Karniadakis's model with a first-order model slip boundary condition, which incorporates a tan function, causing the AGP to fluctuate with K_n, while B-K's model with a first-order model slip boundary condition is also valid at low to moderate values of K_n [24]. In Asana et al.'s and Xiong et al.'s organic permeability models, the AGP remains constant when $K_n > 1$ and is not related to K_n. These models neglect the phase behavior effect on gas properties, and the gas property values are treated as constants. However, in our derived model, the comprehensive effects of the flow regime, stress dependence, phase behavior, and real gas on the AGP are incorporated. Therefore, the gas viscosity and compressibility factor properties vary with pressure; these differences cause the organic AGP to decrease as K_n increases [49]. Additionally, the stress dependence, phase behavior, real gas effects, and water film effect are considered in the presented model, causing the organic nanopore AGP to be smaller than those of Asana et al.'s and Xiong et al.'s models.

4. Results and Discussion

In this section, we further analyze the effects of the storage medium, stress dependence, real gas, surface diffusion, and water storage on AGP. The basic parameters are listed in Table 2.

4.1. Storage Medium and Pore Size. Figure 4 shows that the AGP in organic/inorganic pores with sizes of 2 nm, 20 nm, and 200 nm varies from 1.0 to 50.0 MPa at a temperature of 412 K under reservoir conditions. In general, the AGP generally decreases gradually as the pore pressure decreases and decreases sharply for small pores (i.e., 2 nm and 200 nm). Taking the pore size 2 nm as an example, the AGP can reduce from 0.1197 mD to 0.0007858 mD in organic pores as the pore pressure increases from 1.0 MPa to 50 MPa. However, the AGP of the 200 nm pore remains constant with a pore pressure increase. This difference arises because in the continuum flow regime, the AGP is mainly determined by the pore size. In addition, the AGP in organic pores is usually greater than that in inorganic pores, which is attributed to the absorbed/surface diffusion in organic pores and the water film in inorganic pores. Notably, in the flow transition region, i.e., as the flow regime transitions from transition flow ($K_n > 0.1$) to slip flow ($10^{-3} < K_n < 10^{-1}$), the AGP in inorganic pores is greater than that in organic pores. In Figure 4, the flow transition pore pressure is 1 MPa to

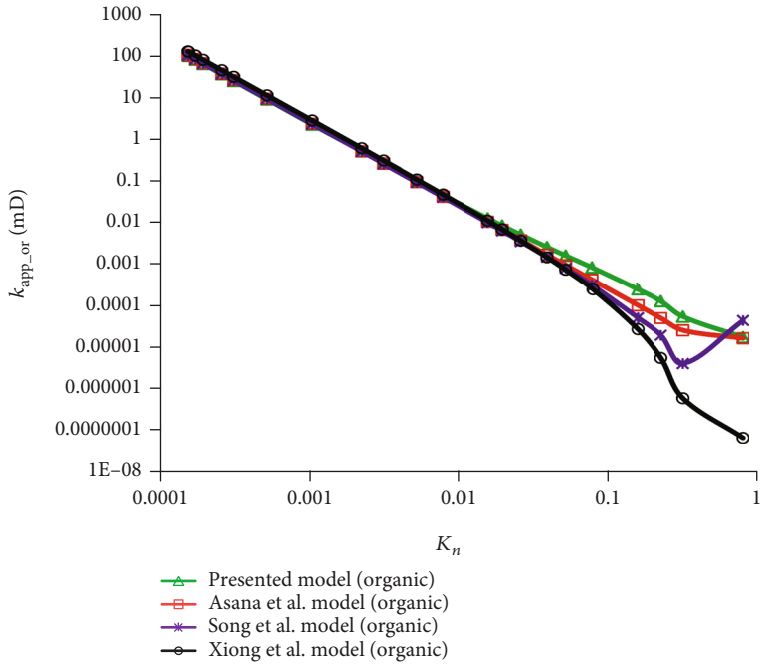

(a) AGP for an organic pore versus K_n

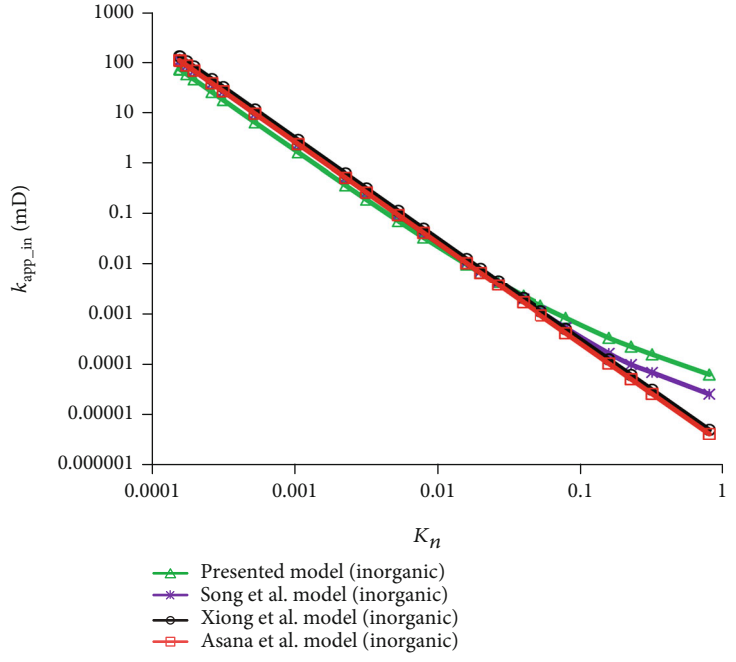

(b) AGP for an inorganic pore versus K_n

Figure 3: Comparison of organic and inorganic matters with other models (p = 30.9 MPa, T = 412 K).

3 MPa for a pore size of 20 nm but 21 MPa to 25 MPa for a pore size of 2 nm.

4.2. Stress Dependence Effect. Figure 5 presents the conditions of considering the stress dependence effect to the AGP in organic nanopores within 2 and 20 nm pores from 1.0 to 50.0 MPa under a temperature of 412 K. The AGP decreases as the effective pressure increases, which is confirmed by the definition of effective pressure. As shown in Figure 6, the deviation in the stress dependence effect for pore sizes of 2 nm and 20 nm, the ratio of change in the AGP to the AGP in the organic pore, varies from -20.45% to -13.69%. This result implies that the stress dependence effect has a profound effect on the AGP and cannot be neglected. Notably, the stress dependence effect usually reduces the AGP under any pressure, except at a certain pressure stage, as shown for a pore size of 2 nm between 21 MPa and 25 MPa, because the AGP increases as the pore pressure decreases, and the slip flow parameters also change with pore pressure. Assuming that the in situ stress is constant, these changes

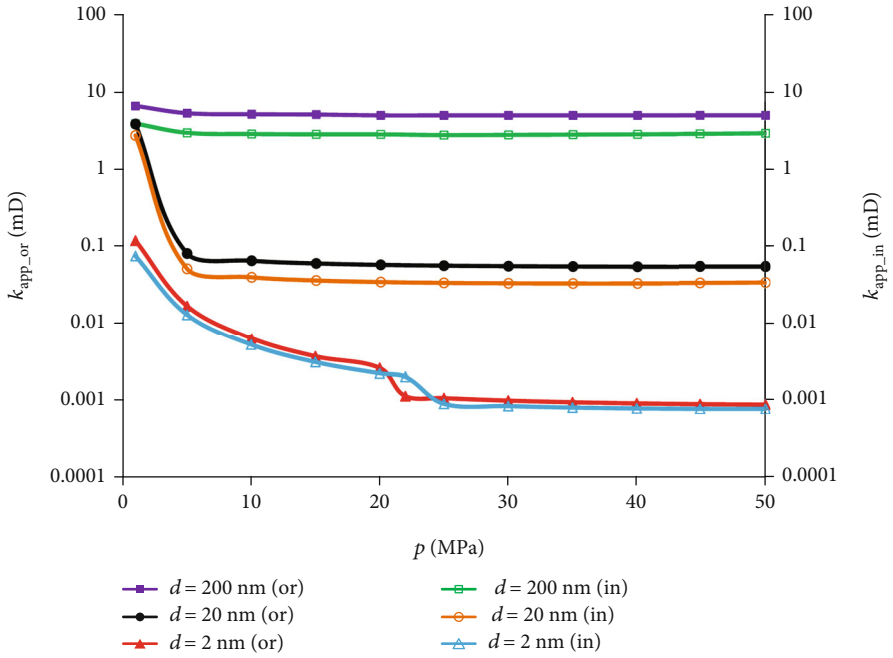

Figure 4: AGP comparison between organic and inorganic pores with different sizes under reservoir conditions.

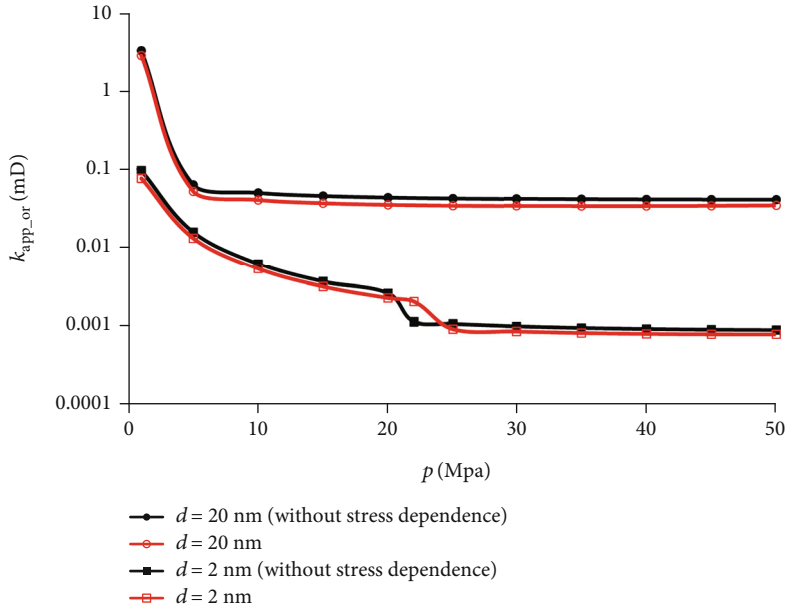

Figure 5: Organic pore AGP curves with and without considering the stress dependence.

have two consequences: (1) The permeability will increase with the increase in pore pressure (i.e., the effective pore pressure will decrease). (2) The slip flow will increase with increasing pore pressure, thus decreasing the AGP. Therefore, the final permeability value is determined by the interplay of the effective stress and slip flow effect.

4.3. Real Gas Effect. Figure 7 shows the organic pore AGP comparison between real gas and ideal gas as the pressure increases from 1 MPa to 50 MPa for pore sizes of 2 nm and 20 nm. The effect of real gas has a dramatic influence on the organic pore AGP calculated by the ideal gas model under pressures lower than 30.0 MPa for a pore size of 20 nm and for pressures greater than 30 MPa for a pore size of 2 nm (Figure 8). This result occurs because the real gas compressibility varies with pressure and temperature, while the gas compressibility is assumed to be constant for an ideal gas [50]. Notably, the real gas effect can dramatically reduce the AGP from that calculated by the ideal gas model at 50 MPa for the 2 nm pore size because the continuum flow regime in 2 nm pores and the increased viscosity at high pressures have a profound effect on gas permeability. According to

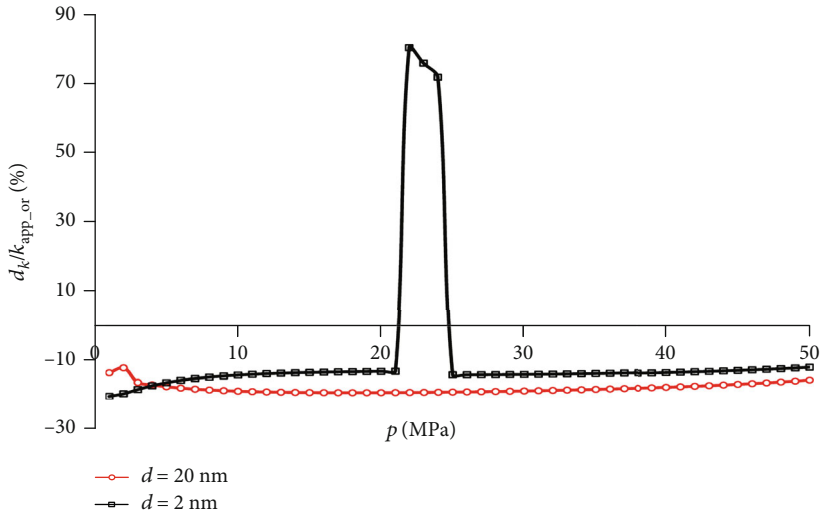

Figure 6: Curves of the ratio of change in the AGP to the AGP in the organic pore without considering the stress dependence.

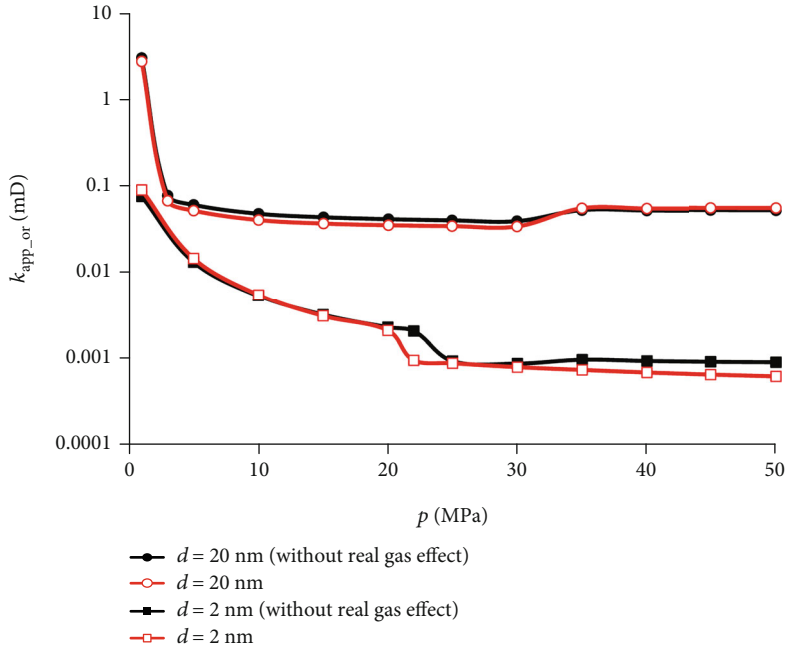

Figure 7: Organic pore AGP curves with and without considering the real gas effect.

Equations (29)–(36), the real gas viscosity can increase from 1.85×10^{-5} to 2.62×10^{-5} Pa·s (the relative error is 44.4%) as the pore pressure increases from 1.0 to 50 MPa at 323 K. Clearly, the real gas effect cannot be neglected.

4.4. Surface Diffusion Effect. Figure 9 shows the difference in the AGP in organic pores between considering surface diffusion and not considering surface diffusion at diameters of 2 nm and 20 nm as the pressure changes from 1 MPa to 50 MPa. It is obvious that the surface diffusion effect on organic pore permeability decreases as the pore pressure decreases. As shown in Figure 10, the surface effect exerts a profound influence on the organic permeability at the 2 nm pore size for the entire range of pressures, especially for low pressures. The surface diffusion effect has little influence on the reduction in the 20 nm pore size under high pressure because the surface diffusion permeability is determined by the surface diffusion coefficient and the adsorbed gas maximum adsorption concentration to the squared pore pressure, C_{smax}/p^2. Obviously, the increase in C_{smax}/p is greater than the increase in gas maximum adsorption concentration as the pore pressure increases. In addition, the surface diffusion contribution to the organic pore permeability increases as the pore radius decreases because under the same formation pressure, the ratio of absorbed gas area to the total pore area in a section increases as the pore size decreases. Under the condition of a pore size of 2 nm, the surface diffusion permeability deviation ranges from 74.85% to 1.67% for the pore

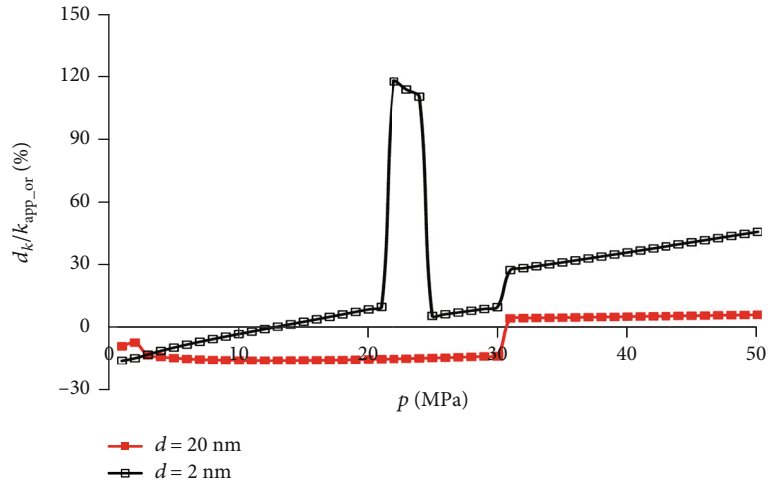

Figure 8: Curves of the ratio of change in the AGP to the AGP in the organic pore without considering the real gas effect.

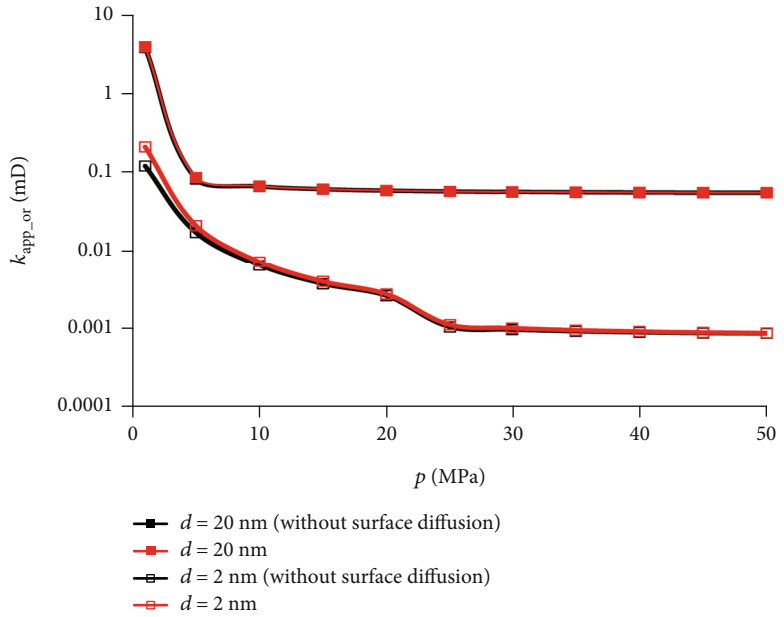

Figure 9: Organic pore AGP curves in with and without considering the surface diffusion effect.

pressure increase from 1 MPa to 50 MPa, revealing that surface diffusion should be considered under low pressures. When the pore pressure is greater than 10 MPa in the 20 nm pore, the surface diffusion contribution is smaller than 1.0%, which can be ignored.

4.5. Water Storage Effect. The gas permeability results of our models for different inorganic pore sizes with water storage are compared in Figure 11. The AGP at a low water saturation is generally larger than that at a high water saturation, which is consistent with the findings of other studies [51, 52]. In our model, according to Equation (28), the gas flow radius decreases as the water saturation increases. However, the AGP does not always decrease as the water saturation increases for a small pore size. Figure 11 indicates a step change relationship between k_{app_in} and s_w; namely, k_{app_in} first decreases with the increase in s_w at a low s_w but then increases after s_w reaches a critical value. According to Equation (26), the increase in s_w implies a decrease in the nanopore flow radius. For the gas flow regime satisfying continuum flow, k_{app_in} decreased as water saturation increases, according to Equation (39). As s_w further increases, the effective pore size decreases and K_n increases, and the flow regime of the gas transfers from continuum flow to slip flow. The decrease in r_{eff_in} does not imply a decrease in the gas k_{app}. Based on Equation (42), the water saturation effect on gas k_{app_in} can be divided into two parts: r_{eff_in} and b_k. The effective flow radius of the inorganic pore decreases,

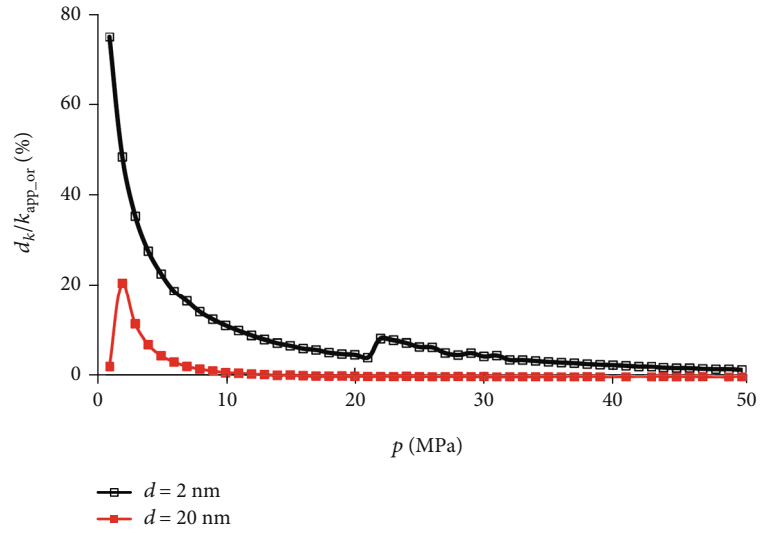

Figure 10: Curves of the ratio of change in the AGP to the AGP in the organic pore without considering the surface diffusion effect.

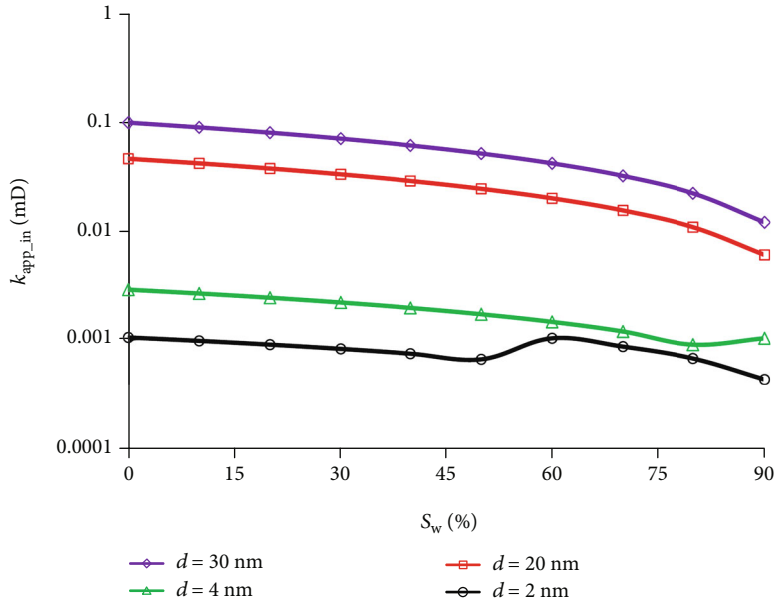

Figure 11: Gas permeability at different water saturations for different pore sizes.

while the gas slippage factor b_k increases under higher water saturation conditions. Whether k_{app_in} increases or decreases with s_w depends on the coupled effect of r_{eff_in} and b_k. k_{app_in} clearly exhibits a turning point as the water saturation increases to 50% for a pore size of 2 nm because the gas flow states have changed from a continuous flow regime to a slip flow regime. However, k_{app_in} exhibits no turning point with s_w for a pore size of 20 or 30 nm within the continuum flow regime for all the water saturations investigated.

5. Summary and Conclusions

Shale organic/inorganic pore analytical AGP models are derived in this paper. The presented AGP model results match well with the results calculated via the models of Xiong et al., Asana et al., and Song et al. Unlike the earlier models, the presented models consider absorption, stress dependence, water storage, and real gas effects on organic/inorganic gas transport comprehensively for the entire flow regime. The results demonstrate that the AGP generally decreases gradually as the pore pressure decreases but that the decrease is sharp in small pores. Generally, the AGP usually decreases when taking the stress dependence effect into account. In real situations, the final permeability value is determined by the interplay of the effective stress and slip flow effects. Notably, the AGP decreases dramatically when considering the real gas effect at 50 MPa in a 2 nm pore size. Clearly, the surface effect exerts a profound influence on the

organic permeability of the 2 nm pore for the entire range of pressures investigated, especially at low pressures. The AGP usually decreases as the water saturation increases for high-water saturation conditions, considerably reducing the effective gas pathways. For a small pore size at the critical high-water saturation, k_{app} might increase suddenly as the flow regime changes from continuum flow to slip flow.

Nomenclature

Roman Alphabet

b_k: Gas slip factor (MPa)
C_A: Constants (-)
C_{smax}: Maximum adsorption concentration (mol/m^3)
d: Effective radius of the nanopores (m^2)
d_m: Gas molecule diameter (-)
D_k: Knudsen diffusion constant (m^2/s)
$D_{eff\text{-}k}$: Effective Knudsen diffusion constant (m)
D_f: Pore wall fractal dimension (-)
D_s: Coefficient surface diffusion (m^2/s)
$J_{vicious}$: The continuum flow volume flux (kg/(m^2·s))
J_{slip}: Volume flux for the slip regime (kg/(m^2·s))
$J_{Knudsen}$: Volume flux for the Knudsen regime (kg/(m^2·s))
J_t: Volume flux (kg/(m^2·s))
$J_{surface}$: Volume flux for the surface diffusion (kg/(m^2·s))
k_B: Boltzmann constant (-)
K_n: Knudsen number (-)
k_∞: Intrinsic permeability (m^2)
$K_{nViscous}$: K_n when the flow regime transfers from viscous to diffusion flow (-)
K_d: Intermediate variable of the viscosity calculation (-)
k_{slip}: Slip flow regime AGP (m^2)
$k$app_in1: The apparent permeability of shale inorganic pores when the fluid flow pattern is continuum flow (m^2)
$k$app_in2: The apparent permeability of shale inorganic pores when the fluid flow regime is slip flow (m^2)
$k$app_in3: The apparent permeability of shale inorganic pores when the fluid flow regime is free molecule flow (m^2)
$k$app_in4: The apparent permeability of shale inorganic pores when the fluid flow regime is transition flow (m^2)
$k$app_or1: The apparent permeability of shale organic pores when the fluid flow pattern is continuum flow (m^2)
$k$app_or2: The apparent permeability of shale organic pores when the fluid flow regime is slip flow (m^2)
$k$app_or3: The apparent permeability of shale organic pores when the fluid flow regime is free molecule flow (m^2)
$k$app_or4: The apparent permeability of shale organic pores when the fluid flow regime is transition flow (m^2)
l_c: Capillary length (-)
M: Molar mass (kg/mol)
p: Pore pressure (MPa)
p_{aver}: Gas phase mean pressure (MPa)
p_L: Langmuir pressure (MPa)
p_c: Confining pressure (MPa)
p_e: Effective stress (m)
p_r: Pseudopressure (-)
q: Material constants (-)
r: Nanopore radius (m)
R: Universal gas constant (J/(mol·K))
r_{ef_or}: Effective pore flow radius considering gas desorption (m)
r_{e_or}: Original pore radius of the organic pore (m)
r_{ef}: Effective flow radius considering the stress dependence effect (m)
r_{e_in}: Hydrodynamic radius for inorganic pores taking the stress dependence effect into account (m)
r_{eff_in}: Inorganic pore effective flow radius considering the stress dependence effect and water storage characteristics (m)
r_{eff_or}: Effective flow radius for organic pores considering gas desorption and the stress dependence effect (m)
S: Constants (-)
s: Material constants (-)
S_w: Shale pore water saturation, dimensionless (-)
T: Formation temperature (K)
T_r: Pseudotemperature (-)
T_c: Critical temperature (K)
V: Adsorbed gas volume per shale unit weight under standard conditions (m^3/kg)
V_L: Langmuir volume under standard conditions (m^3/kg)
v_w: Bound water volume (m)
v_p: Bound water pore volume (m^3)
X: Density multiplication factor (-)
Y: Density index (-)
Z: Gas compressibility factor (-)

Greek Alphabet

λ: Molecular mean free path (m)
δ: Gas molecule collision diameter (m)
ρ: Gas density (kg/m^3)
μ: Gas viscosity (Pa·s)
μ_{eff}: Effective viscosity of the gas transport in nanopores (Pa·s)
∇: Pressure gradient operator symbol (-)
α: Tangential momentum accommodation coefficient (TMAC) (-)
ε: Contribution coefficient term (-)
θ: Gas coverage under certain pressures (-)
φ: Porosity under the effective stress (-)
φ_e: Porosity at atmospheric pressure (-).

Data Availability

The authors can make data available on request through a data access committee, institutional review board, or the authors themselves.

Conflicts of Interest

The authors declare that there are no conflicts of interest in association with the reporting of the case or publication of this article.

Acknowledgments

This work was supported by the Sichuan Science and Technology Plan Project (grant number 2020YJ013), the Natural Science Foundation of China (grant numbers 51504203, 51525404, and 51374178), and the National Key and Development Program of China (grant number 2017ZX05037-004).

References

[1] G. R. Chalmers, R. M. Bustin, and I. M. Power, "Characterization of gas shale pore systems by porosimetry, pycnometry, surface area, and field emission scanning electron microscopy/-transmission electron microscopy image analyses: examples from the Barnett, Woodford, Haynesville, Marcellus, and Doig units," *AAPG Bulletin*, vol. 96, no. 6, pp. 1099–1119, 2012.

[2] Z. Gao, Y. Fan, Q. Xuan, and G. Zheng, "A review of shale pore structure evolution characteristics with increasing thermal maturities," *Advances in Geo-Energy Research*, vol. 4, no. 3, pp. 247–259, 2020.

[3] U. Kuila, D. K. Mccarty, A. Derkowski, T. B. Fischer, T. Topór, and M. Prasad, "Nano-scale texture and porosity of organic matter and clay minerals in organic-rich mudrocks," *Fuel*, vol. 135, pp. 359–373, 2014.

[4] Z. Tao, X. Li, S. Zheng et al., "An analytical model for relative permeability in water-wet nanoporous media," *Chemical Engineering Science*, vol. 174, pp. 1–12, 2017.

[5] H. Song, M. Yu, W. Zhu et al., "Numerical investigation of gas flow rate in shale gas reservoirs with nanoporous media," *International Journal of Heat & Mass Transfer*, vol. 80, pp. 626–635, 2015.

[6] L. He, H. Mei, X. Hu, M. Dejam, Z. Kou, and M. Zhang, "Advanced flowing material balance to determine original gas in place of shale gas considering adsorption hysteresis," *SPE Reservoir Evaluation & Engineering*, vol. 22, pp. 1–11, 2019.

[7] M. Wei, Y. Duan, M. Dong, Q. Fang, and M. Dejam, "Transient production decline behavior analysis for a multi-fractured horizontal well with discrete fracture networks in shale gas reservoirs[J]," *Journal of Porous Media*, vol. 22, no. 3, pp. 343–361, 2019.

[8] G. Xu, H. Yin, H. Yuan, and C. Xing, "Decline curve analysis for multiple-fractured horizontal wells in tight oil reservoirs," *Advances in Geo-Energy Research*, vol. 4, no. 3, pp. 296–304, 2020.

[9] J. P. Korb, B. Nicot, A. Louis-Joseph, S. Bubici, and G. Ferrante, "Dynamics and wettability of oil and water in oil shales," *Journal of Physical Chemistry C*, vol. 118, pp. 23212–23218, 2015.

[10] M. Xu and H. Dehghanpour, "Advances in understanding wettability of gas shales," *Energy & Fuels*, vol. 28, no. 7, pp. 4362–4375, 2014.

[11] W. Song, "Apparent gas permeability in an organic-rich shale reservoir," *Fuel*, vol. 181, pp. 973–984, 2016.

[12] F. Javadpour, D. Fisher, and M. Unsworth, "Nanoscale gas flow in shale gas sediments," *Journal of Canadian Petroleum Technology*, vol. 46, 2007.

[13] G. A. Bird and J. Brady, *Molecular Gas Dynamics and the Direct Simulation of Gas Flows, Vol 5*, Clarendon Press Oxford, 1994.

[14] S. Roy, R. Raju, H. F. Chuang, B. A. Cruden, and M. Meyyappan, "Modeling gas flow through microchannels and nanopores," *Journal of Applied Physics*, vol. 93, no. 8, pp. 4870–4879, 2003.

[15] W. J. Shen, F. Q. Song, X. Hu, G. M. Zhu, and W. Y. Zhu, "Experiental study on flow characteristics of gas transport in micro- and nanoscale pores," *Scientific Reports*, vol. 9, article 10196, 2019.

[16] J. Wang, H. Luo, H. Liu, F. Cao, Z. Li, and K. Sepehrnoori, "An integrative model to simulate gas transport and production coupled with gas adsorption, non-Darcy flow, surface diffusion, and stress dependence in organic-shale reservoirs," *SPE Journal*, vol. 22, pp. 244–264, 2019.

[17] X. Qiu, S. P. Tan, M. Dejam, and H. Adidharma, "Isochoric measurement of the evaporation point of pure fluids in bulk and nanoporous media using differential scanning calorimetry," *Physical Chemistry Chemical Physics*, vol. 22, no. 13, pp. 7048–7057, 2020.

[18] X. Qiu, S. P. Tan, M. Dejam, and H. Adidharma, "Experimental study on the criticality of a methane/ethane mixture confined in nanoporous media," *Langmuir*, vol. 35, no. 36, pp. 11635–11642, 2019.

[19] G. E. K. Ali Beskok, "Report: a model for flows in channels, pipes, and ducts at micro and nano scales," *Microscale Thermophysical Engineering*, vol. 3, no. 1, pp. 43–77, 1999.

[20] G. Karniadakis, A. Beskok, and M. Gad-El-Hak, "Micro Flows: Fundamentals and Simulation," *Applied Mechanics Reviews*, vol. 55, no. 4, p. 76, 2020.

[21] F. Civan, "Effective correlation of apparent gas permeability in tight porous media," *Transport in Porous Media*, vol. 82, no. 2, pp. 375–384, 2010.

[22] S. Zheng, J. Shi, K. Wu et al., "Transport capacity of gas confined in nanoporous ultra-tight gas reservoirs with real gas effect and water storage mechanisms coupling," *International Journal of Heat & Mass Transfer*, vol. 126, pp. 1007–1018, 2018.

[23] D. Chai, G. Yang, Z. Fan, and X. Li, "Gas transport in shale matrix coupling multilayer adsorption and pore confinement effect," *Chemical Engineering Journal*, vol. 370, pp. 1534–1549, 2019.

[24] M. R. Shahri, R. Aguilera, and A. Kantzas, "A new unified diffusion-viscous flow model based on pore level studies of tight gas formations," *SPE Journal*, vol. 18, pp. 38–49, 2012.

[25] H. Adzumi, "Studies on the flow of gaseous mixtures through capillaries. II. The molecular flow of gaseous mixtures," *Bulletin of the Chemical Society of Japan*, vol. 12, pp. 285–291, 1937.

[26] F. Javadpour, "Nanopores and apparent permeability of gas flow in mudrocks (shales and siltstone)," *Journal of Canadian Petroleum Technology*, vol. 48, pp. 16–21, 2013.

[27] H. Darabi, A. Ettehad, F. Javadpour, and K. Sepehrnoori, "Gas flow in ultra-tight shale strata," *Journal of Fluid Mechanics*, vol. 710, pp. 641–658, 2012.

[28] K. Wu, Z. Chen, and X. Li, "Real gas transport through nanopores of varying cross-section type and shape in shale gas reservoirs," *Chemical Engineering Journal*, vol. 281, pp. 813–825, 2015.

[29] F. Zeng, F. Peng, J. Guo, Z. Rui, and J. Xiang, "Gas mass transport model for microfractures considering the dynamic variation of width in shale reservoirs," *SPE Reservoir Evaluation & Engineering.*, vol. 22, no. 4, pp. 1265–1281, 2019.

[30] F. Zeng, F. Peng, J. Guo et al., "Gas transport study in the confined microfractures of coal reservoirs," *Journal of Natural Gas Science and Engineering*, vol. 68, article 102920, 2019.

[31] P. C. Carman, *Flow of Gases through Porous Media*, Academic Press Inc., Butterworths Scientific Publications, New York, London, 1956.

[32] D. J. Ross and R. M. Bustin, "Characterizing the shale gas resource potential of Devonian–Mississippian strata in the Western Canada sedimentary basin: application of an integrated formation evaluation," *AAPG Bulletin*, vol. 92, no. 1, pp. 87–125, 2008.

[33] D. J. Soeder, "Porosity and permeability of eastern Devonian gas shale," *SPE Formation Evaluation*, vol. 3, pp. 116–124, 2013.

[34] G. Karniadakis, A. Beskok, and N. Aluru, "Microflows and Nanoflows. Fundamentals and Simulation. With a Foreword by Chih-Ming Ho," in *Interdisciplinary Applied Mathematics*, vol. 29, Springer, New York, 2005.

[35] H. Smith, "Transport Phenomena," *Applied Mechanics Reviews*, vol. 55, no. 1, pp. R1–R4, 2003.

[36] L. Klinkenberg, "The permeability of porous media to liquids and gases," in *Paper presented at: drilling and production practice*, American Petroleum Institute, 1941.

[37] M. A. Jingsheng, P. J. Sanchez, W. U. Kejian, D. Gary, and Z. Jiang, "A pore network model for simulating non-ideal gas flow in micro- and nano-porous materials," *Fuel*, vol. 116, pp. 498–508, 2014.

[38] J. G. Choi, D. D. Do, and H. D. Do, "Surface diffusion of adsorbed molecules in porous media: monolayer, multilayer, and capillary condensation regimes," *Industrial & Engineering Chemistry Research*, vol. 40, no. 19, pp. 4005–4031, 2001.

[39] K. Wu, Z. Chen, X. Li, C. Guo, and M. Wei, "A model for multiple transport mechanisms through nanopores of shale gas reservoirs with real gas effect–adsorption-mechanic coupling," *International Journal of Heat & Mass Transfer*, vol. 93, pp. 408–426, 2016.

[40] M. Coppens, "The effect of fractal surface roughness on diffusion and reaction in porous catalysts – from fundamentals to practical applications," *Catalysis Today*, vol. 53, no. 2, pp. 225–243, 1999.

[41] T. Veltzke and J. Thöming, "An analytically predictive model for moderately rarefied gas flow," *Journal of Fluid Mechanics*, vol. 698, pp. 406–422, 2012.

[42] H. Adzumi, "Studies on the flow of gaseous mixtures through capillaries. III. The flow of gaseous mixtures at medium pressures," *Bulletin of the Chemical Society of Japan*, vol. 12, pp. 292–303, 1937.

[43] M. Rahmanian, R. Aguilera, and A. Kantzas, "A new unified diffusion–viscous-flow model based on pore-level studies of tight gas formations," *SPE Journal*, vol. 18, no. 1, pp. 37–47, 2013.

[44] J. J. Dong, J. Hsu, W. J. Wu, T. Shimamoto, Hung, and J. Hao, "Stress-dependence of the permeability and porosity of sandstone and shale from TCDP Hole-A," *International Journal of Rock Mechanics & Mining Sciences*, vol. 47, no. 7, pp. 1141–1157, 2010.

[45] F. Civan, C. S. Rai, and C. H. Sondergeld, "Shale-gas permeability and diffusivity inferred by improved formulation of relevant retention and transport mechanisms," *Transport in Porous Media*, vol. 86, no. 3, pp. 925–944, 2011.

[46] H. Tran and A. Sakhaee-Pour, "Viscosity of shale gas," *Fuel*, vol. 191, pp. 87–96, 2017.

[47] X. Xinya, D. Deepak, M. Villazon, R. F. Sigal, and F. Civan, "A fully-coupled free and adsorptive phase transport model for shale gas reservoirs including non-Darcy flow effects," in *SPE Annual Technical Conference and Exhibition*, San Antonio, Texas, USA, 2012.

[48] W. Asana and I. Y. Akkutlu, "Permeability of organic-rich shale," *SPE Journa*, vol. 20, no. 16, pp. 1384–1496, 2015.

[49] L. Geng, G. Li, P. Zitha, S. Tian, S. Mao, and X. Fan, "A diffusion–viscous flow model for simulating shale gas transport in nano-pores," *Fuel*, vol. 181, pp. 887–894, 2016.

[50] K. Wu, X. Li, C. Guo, C. Wang, and Z. Chen, "A unified model for gas transfer in nanopores of shale-gas reservoirs: coupling pore diffusion and surface diffusion," *Spe Journal*, vol. 21, 2016.

[51] R. K. Estes and P. F. Fulton, "Gas slippage and permeability measurements," *Journal of Petroleum Technology*, vol. 18, no. 10, pp. 69–73, 1956.

[52] Q. Wu, B. Bai, Y. Ma, J. T. Ok, X. Yin, and K. Neeves, "Optic imaging of two-phase-flow behavior in 1D nanoscale channels," *SPE Journal*, vol. 19, no. 5, pp. 793–802, 2014.